

# Intensity of singular stress fields of wedge-shaped defect in human tooth due to occlusal force before and after restoration with composite resins

Proc IMechE Part H:  
*J Engineering in Medicine*  
1–16  
© IMechE 2017  
Reprints and permissions:  
sagepub.co.uk/journalsPermissions.nav  
DOI: 10.1177/0954411917701495  
journals.sagepub.com/home/pih  


Ker-Kong Chen<sup>1</sup>, Nao-Aki Noda<sup>2</sup>, Kiyoshi Tajima<sup>3</sup>, Yoshikazu Sano<sup>2</sup> and Yasushi Takase<sup>2</sup>

## Abstract

Wedge-shaped defects are frequently observed on the cervical region of the human tooth. Previously, most studies explained that improper tooth-brushing causes such defects. However, recent clinical observation suggested that the repeated stress due to occlusal force may induce the formation of these wedge-shaped defects. In this study, therefore, two-dimensional human tooth models are considered with and without a wedge-shaped defect by applying the finite element method. To evaluate large stress concentrations accurately, a method of analysis is discussed in terms of the intensity of singular stress fields appearing at the tip of the sharp wedge-shaped defect. The effects of the position and direction of occlusion on the intensity of singular stress fields are discussed before and after restoration with composite resins.

## Keywords

Finite element, fracture mechanics, wedge-shaped defect, modeling/simulation, strain analysis, stress analysis

Date received: 9 May 2016; accepted: 3 March 2017

## Introduction

Wedge-shaped defects as shown in Figure 1 are frequently observed on the cervical region of the human tooth. Such types of defects are more frequently observed in aging people. Therefore, to establish a remedy will become more important in aging society, which is appearing in Japan and will appear in many other countries in the near future.

As an early stage of the research, Miller<sup>1</sup> proposed that the wedge-shaped defect is caused by hard toothbrush and that was accepted for a long time. Whereas Bream et al.<sup>2</sup> found wedge-shaped defect at the region hard to be brushed in human mouth. Similarly, Graehn and Muller<sup>3</sup> confirmed wedge-shaped defect in the animal tooth. Tanaka et al.<sup>4</sup> reported that the wedge-shaped defect exists in the ancients who had not used toothbrush. Those studies suggested that improper toothbrush cannot be the only reason for wedge-shaped defects. Lee and Eakle<sup>5</sup> suggested that when occlusion is not ideal, the tensile stress due to lateral forces may disrupt the chemical bonds of the crystalline structure of enamel and dentin. Recently, Chen et al.<sup>6</sup> used the

maxillary second premolar and measured the strain to find out the potential relationship between occlusion and wedge-shaped defect.

Table 1 shows the number of individual types of fractures including wedge-shaped defects and the total number of teeth.<sup>7</sup> In this study, 304 extracted maxillary premolars were investigated. Here, the shapes of defects are classified into three types, that is, (1) ditch type, which is minute and can only be detected through microscope; (2) angular type, whose two faces have angular corner; and (3) round type, which shapes curved surface. Those defects were found in 198

<sup>1</sup>School of Dentistry, College of Dental Medicine, Kaohsiung Medical University, Kaohsiung, Taiwan, R.O.C.

<sup>2</sup>Department of Mechanical Engineering, Kyushu Institute of Technology, Fukuoka, Japan

<sup>3</sup>Division of Biomaterials, Kyushu Dental College, Fukuoka, Japan

## Corresponding author:

Nao-Aki Noda, Department of Mechanical Engineering, Kyushu Institute of Technology, Sensui-Cho 1-1, Tobata-Ku, Kitakyushu-Shi, Fukuoka 804-8550, Japan.

Email: noda@mech.kyutech.ac.jp

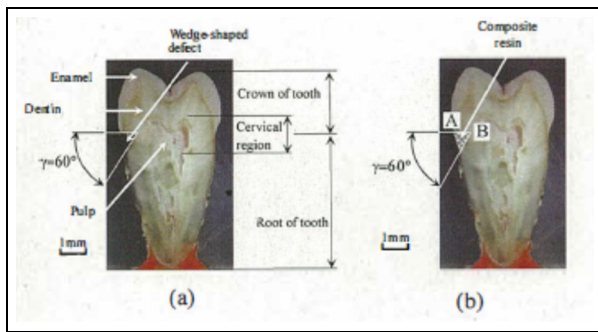


**Figure 1.** Wedge-shaped defect in human tooth: (a) before and (b) after restoration with composite resins.

**Table 1.** Number of individual types of fractures and the total number of teeth.<sup>7</sup>

Type	Buccal	Lingual
Ditch	41	9
Angular	66	5
Round	78	22
Total	185	36

(65.1%) teeth of 304 at the buccal and lingual cervical regions. It was found in 162 teeth of 198 at only the buccal cervical regions, in 13 teeth at only the lingual cervical regions, and in 23 teeth at both the buccal and lingual. The number of occurrence is 185 teeth in buccal and 36 teeth in lingual as shown in Table 1.

Figure 2(a) and (b) shows two models considered by Kuroe et al.<sup>8,9</sup> as extreme cases for cervical lesion. The real shape of defect is between the shapes of Figure 2(a) and (b). However, it is too difficult to define the typical shape and size, so the extreme models shown in Figure 2(a) and (b) have been used. Generally, it is said that V-shaped defect as shown in Figure 2(a) appears when the effect of occlusal force is larger, and round-type defect as shown in Figure 2(b) is formed from tooth-brushing effects. Here, the model of Figure 2(a) has singular stress; however, the singular stress field (intensity of singular stress field (ISSF)) has not been discussed in previous studies. Since ISSFs cannot be

calculated easily, in this article, the method of analysis will be explained. Then the effect of occlusal force on the ISSFs will be discussed.

In this study, the effect of occlusal force on the ISSFs will be mainly considered by the application of finite element method (FEM). Generally, it has been told that the remedy for wedge-shaped defects is more difficult than the remedy for dental caries. Therefore, desirable occlusal force will be proposed from the viewpoint of mechanics. Figure 2(c) shows the two-dimensional (2D) model of wedge-shaped defect considered in this study. The singular stress should be considered along the bisector of corner B. Figure 2(d) shows the 2D model of the wedge-shaped defect after restoration with composite resins. The singular stress should be considered at corner B and also at the interfaced end A. In the previous studies, fracture mechanics approach was used in several references for human teeth<sup>10–15</sup> and human bone.<sup>16–24</sup> Usually, fracture mechanics assumes crack models. In this study, however, the FEM is applied to a general model of wedge-shaped defect. Then the ISSFs will be calculated, and the effect of the occlusal force on the ISSF will be discussed before and after restoration with composite resins.

## Materials and methods

### Mesh-independent technique to analyze the ISSFs

In this study, the ISSFs have been calculated accurately for the wedge-shaped defect as shown in Figure 2(c). Since the shape and structure of human tooth are complex as shown in Figure 1, the numerical solution will be discussed when the FEM is applied to 2D problems of wedge-shaped defects. To confirm the accuracy of the proposed method, the exact solution obtained by the body force method (BFM) will be used as a reference solution. Since FEM error is controlled by the mesh size around the corner, the error can be eliminated by applying the same mesh to be the unknown problem and the reference problem.<sup>25,26</sup> The BFM has been applied to a lot of stress concentration problems<sup>27,28</sup> including wedge-shaped defects.<sup>29–31</sup> The solution in the

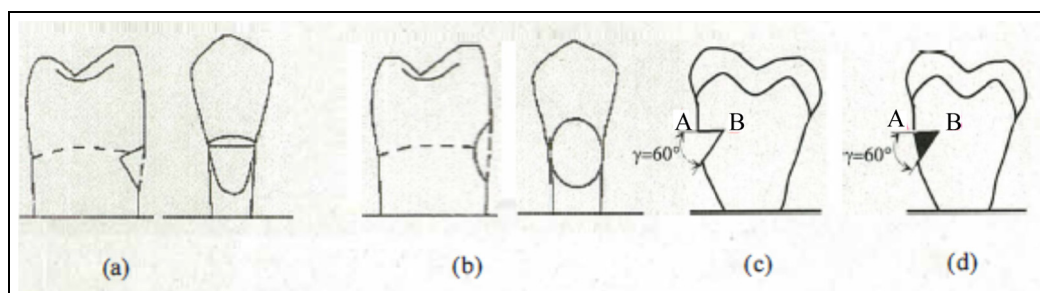


**Figure 2.** Two models (a and b) considered by Kuroe et al. as extreme cases for cervical lesion<sup>8,9</sup> and two 2D models (c and d) considered in this study: (a) wedge-shaped defect, (b) round shaped defect, (c) 2D wedge-shaped defect, and (d) 2D wedge-shaped defect after restoration.

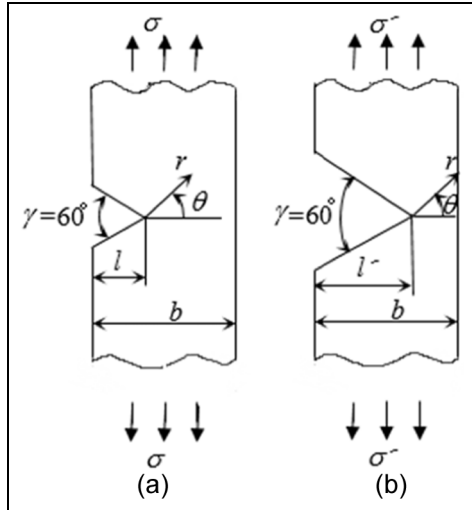


**Figure 3.** Sharp notches in a strip when notch depth (a)  $l/b \leq 0.5$  and (b)  $l'/b \geq 0.5$ .

BFM is obtained by the superposition of fundamental solution so as to satisfy a given boundary condition. By means of these fundamental solutions, all problems can be solved in principle. The detail of the BFM is indicated in the previous studies.<sup>32–35</sup>

First, the wedge-shaped notch whose opening angle  $\gamma = 30^\circ$  in a strip is considered. As shown in Figure 3(a) and (b), different notch dimensions are considered. The ISSFs have been calculated very accurately by Chen and Nisitani<sup>27</sup> for  $l/b \leq 0.5$  by applying the BFM. In the FEM analysis, however, the exact singular stress field cannot be given from finite numbers of elements. Since the error due to the finiteness of the division mainly depends on the mesh around the corner of the notch,<sup>36</sup> if the ISSFs are equal for Figure 3(a) and (b) by adjusting  $\sigma$  and  $\sigma'$ , the stress  $\sigma_{\theta, FEM}^{(b)}$  is also nearly equal.

In other words, if the mesh pattern around the notch corner is the same, the value of  $K_{I, \lambda_1}^{(b)} / \sigma_{\theta, FEM}^{(b)}$  is constant independent of the dimension of the notch. To calculate mode II stress intensity factors,  $\tau_{r\theta, FEM}^*$  can be considered in a similar way. Namely, we have equation (1)

$$\frac{\sigma_{\theta, FEM}^{(b)}}{\sigma_{\theta, FEM}^{(a)}} = \frac{K_{I, \lambda_1}^{(b)}}{K_{I, \lambda_1}^{(a)}} \quad (1a)$$

$$\frac{\tau_{r\theta, FEM}^{(b)}}{\tau_{r\theta, FEM}^{(a)}} = \frac{K_{II, \lambda_2}^{(b)}}{K_{II, \lambda_2}^{(a)}} \quad (1b)$$

The validity of equation (1) has been confirmed by the previous studies, for example, in crack problems,<sup>37</sup> notched problems,<sup>29</sup> and inclusion problems.<sup>30</sup> In this equation, the superscripts  $a$  and  $b$  indicate the values of the problems in Figure 3(a) and (b), for example, the solutions when  $l/b = 0.1$  and  $l/b = 0.8$ . Then  $K_{I, \lambda_1}^{(a)}$  and  $K_{I, \lambda_1}^{(b)}$  mean exact ISSFs from Figure 3(a) and (b), and  $\sigma_{\theta, FEM}^{(a)}$ ,  $\sigma_{\theta, FEM}^{(b)}$ ,  $\tau_{r\theta, FEM}^{(a)}$ , and  $\tau_{r\theta, FEM}^{(b)}$  are the stresses

along the bisector of the notch when the FEM is applied to the same problems.

Equation (1) means the ratio of ISSF for two unknown problems can be obtained by applying FEM easily since FEM error can be eliminated using the same mesh pattern. If the exact solution is available for some notch dimensions, the exact ISSF can be obtained for unknown problems.

The dimensionless ISSFs  $F_{I, \lambda_1}^{(a)}$ ,  $F_{I, \lambda_1}^{(b)}$  are defined as in equation (2). Then equation (3) is given from equation (1)

$$K_{I, \lambda_1}^{(a)} = F_{I, \lambda_1}^{(a)} \sigma \sqrt{\pi} l^{1-\lambda_1}, \quad K_{I, \lambda_1}^{(b)} = F_{I, \lambda_1}^{(b)} \sigma' \sqrt{\pi} l'^{1-\lambda_1} \quad (2)$$

$$\frac{\sigma_{\theta, FEM}^{(b)}}{\sigma_{\theta, FEM}^{(a)}} = \frac{F_{I, \lambda_1}^{(b)} \sigma' \sqrt{\pi} l'^{1-\lambda_1}}{F_{I, \lambda_1}^{(a)} \sigma \sqrt{\pi} l^{1-\lambda_1}} \quad (3)$$

If the ISSFs in Figure 3(a) and (b) are equal, we have  $K_{I, \lambda_1}^{(a)} = K_{I, \lambda_1}^{(b)}$ ; then the stress at infinity in Figure 3(b) can be written as equation (4)

$$\sigma' = \sigma \times \frac{F_{I, \lambda_1}^{(a)}}{F_{I, \lambda_1}^{(b)}} \times \frac{l^{1-\lambda_1}}{(l')^{1-\lambda_1}} \quad (4)$$

Therefore, the ISSFs of the problem in question can be given from the FEM results of the problem in question and the reference problem as shown in equation (5)

$$F_{I, \lambda_1}^{(b)} = \sigma_{\theta, FEM}^{(b)} \times \frac{F_{I, \lambda_1}^{(a)}}{\sigma_{\theta, FEM}^{(a)}} \times \frac{\sigma}{\sigma'} \times \frac{l^{1-\lambda_1}}{(l')^{1-\lambda_1}} \quad (5)$$

In the following sections, the ISSFs of Figure 3 will be obtained from equation (5) and compared with the exact solutions. Then the usefulness of the present solution will be confirmed.

### Mesh-independent analysis for sharp V-shaped notches

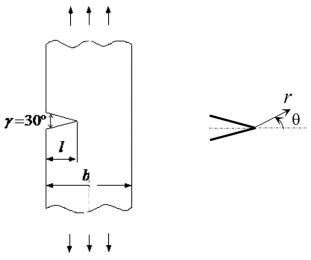
First, mode I-type ISSFs are calculated when  $\gamma = 60^\circ$  and  $\beta = 0^\circ$  in Figure 3 with varying  $l/b = 0.1-0.9$ . Here, the exact value of  $l/b = 0.1$  is used as the reference solution and then the results of  $l/b = 0.2-0.9$  will be calculated by the application of FEM. Table 2 shows the stress distribution  $\sigma_\theta^{(b)}$  along the bisector of the notch when  $l/b = 0.1$  with  $\sigma = 1$  and then the results are used as the reference results as  $\sigma_\theta^{(a)}$ . Here the mesh around the notch corner is the same as Figure 5(b), which is shown later. Also, Table 2 shows the ratio  $\sigma_\theta^{(b)} / \sigma_\theta^{(a)}$  when  $l/b = 0.8$  with  $\sigma = 1$ . As shown in Table 2, the value of  $\sigma_\theta^{(b)} / \sigma_\theta^{(a)}$  is nearly constant. Then the  $F_{I, \lambda_1}$  values are calculated as shown in Table 3 in comparison to the results of the BFM. It is seen that the present solution has four-digit accuracy. The results show that the proposed method provides accurate ISSFs independent of the mesh size. Table 3 shows that FEM error can be eliminated by applying the same mesh pattern to the unknown problem and

**Table 2.** Stress distributions in Figure 3 with confirming equation (1).

$i$	$r/l$	$\sigma_{\theta}^{(a)}$	$\sigma_{\theta}^{(a)} \times r^{1-\lambda_1}$
(a) $\sigma_{\theta}^{(a)} = \sigma_{\theta} _{l/b=0.1, l/b=0.1}$ with $\sigma = 1$			
0	0	34.3679	0
1	0.0412	17.5446	1.1345
2	0.0823	13.0094	1.1885
3	0.1235	10.5938	1.1846
4	0.1646	9.1939	1.1866
5	0.2058	8.2371	1.1882
6	0.2469	7.5326	1.1900
7	0.2881	6.9853	1.1917
8	0.3292	6.5444	1.1934
9	0.3704	6.1794	1.1950
10	0.4115	5.8707	1.1965
(b) $\sigma_{\theta}^{(b)}/\sigma_{\theta}^{(a)} = \sigma_{\theta} _{l/b=0.8}/\sigma_{\theta} _{l/b=0.1}$			
$i$	$r/l$	$\sigma_{\theta}^{(b)}/\sigma_{\theta}^{(a)}$	
0	0	28.1833	
1	0.00514	28.1444	
2	0.01029	28.0995	
3	0.01543	28.0424	
4	0.02058	27.9813	
5	0.02572	27.9179	
6	0.03086	27.8530	
7	0.03601	27.7872	
8	0.04115	27.7205	
9	0.04630	27.6533	
10	0.05144	27.5856	

**Table 3.** Dimensionless ISSF  $K_{I,\lambda_1}$  defined in equation (11) for the sharp notch in a strip when  $\gamma = 30^\circ$  and  $\beta = 0^\circ$ .

$b/l$	FEM $F_{I,\lambda_1}$	BFM $F_{I,\lambda_1}$	FEM error (%)
0.1	1.217	1.217	0.00
0.2	1.400	1.399	0.07
0.3	1.703	1.699	0.23
0.4	2.160	2.157	0.13
0.5	2.888	2.883	0.17
0.6	4.111	—	—
0.7	5.798	—	—
0.8	12.16	—	—
0.9	35.19	—	—



FEM: finite element method; BFM: body force method.

the reference problem. The detailed discussion has been indicated in Zhang et al.<sup>25</sup> and Noda et al.<sup>26</sup>

The present method is found to be useful for deep notches,  $l/b = 0.6-0.9$ , whose results were not given previously.<sup>10</sup>

### Mesh-independent analysis for inclined V-shaped notch

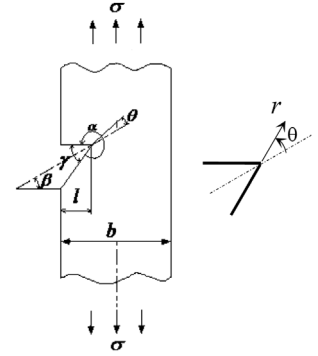
Around an inclined notch as shown in Table 4, the singular stress field can be expressed in terms of mixed mode-type ISSFs as shown in equation (10), (11), and (13). The ISSFs for  $\gamma = 60^\circ$  in a strip are given in Table 4.

Tables 5 and 6 show FEM results for two different inclined notches with the relative notch depth  $l/b = 0.1$  and  $l'/b = 0.2$ . Here, the remote tensile stresses are applied so that the mode I stress intensity factors are equivalent for  $l/b = 0.1$  and  $l'/b = 0.2$  using the results of Figure 4. In addition, the same FE mesh pattern is applied as shown in Figure 5.

Along the bisector of the notch, the stress  $\sigma_{\theta}$  is controlled by  $K_{I,\lambda_1}$  as shown in equation (10), and the stress  $\tau_{r\theta}$  is controlled by  $K_{II,\lambda_2}$  as shown in equations (12) and (13) with  $\theta = 0$ . In Table 5, it is seen that  $\sigma_{\theta} \times r^{1-\lambda_1}$  and  $\tau_{r\theta} \times r^{1-\lambda_2}$  are almost constant, for example, when  $l/b = 0.1$ ,  $\sigma_{\theta} \cong 0.756/r^{1-\lambda_1}$ , and  $\tau_{r\theta} \cong 0.440/r^{1-\lambda_2}$ .

**Table 4.** Dimensionless ISSFs  $K_{I,\lambda_1}, K_{II,\lambda_2}$  defined in equation (11) for the inclined sharp V-notch in a strip when  $\gamma = 60^\circ$ .

$l/b$	$F_{I,\lambda_1}$				$F_{II,\lambda_2}$			
	$\beta$							
$\gamma = 60^\circ$	0°	15°	30°	45°	0°	15°	30°	45°
0.00	1.225	1.176	1.040	0.824	0.000	0.326	0.577	0.684
0.02	1.228	1.181	1.044	0.828	0.000	0.328	0.578	0.687
0.05	1.245	1.197	1.059	0.842	0.000	0.332	0.588	0.698
0.1	1.298	1.249	1.107	0.888	0.000	0.345	0.611	0.734
0.2	1.492	1.437	1.282	1.053	0.000	0.391	0.697	0.858
0.3	1.808	1.746	1.572	1.321	0.000	0.462	0.834	1.060
0.4	2.295	2.224	2.023	1.731	0.000	0.570	1.046	1.369
0.5	3.066	2.980	2.739	2.378	0.000	0.744	1.388	1.857

**Table 5.** Stress distributions along the notch bisector in Figure 4 under the same ISSF  $K_{I,\lambda_1} = K_{I,\lambda_1}^*$  when  $\gamma = 60^\circ$  and  $\beta = 30^\circ$ : (a) when  $l/b = 0.1$  and (b)  $l/b = 0.2$ .

(a) When $l/b = 0.1$ under $K_{I,\lambda_1}^* = F_{I,\lambda_1} \sigma^* \Big _{\sigma^* = 1} \sqrt{\pi l}^{1-\lambda_1} \Big _{l/b = 0.1}$			
$i$	$r/l$	$\sigma_\theta \times r^{1-\lambda_1}$	$\tau_{r\theta} \times r^{1-\lambda_2}$
0	0	0	0
1	0.0412	0.71220	0.34720
2	0.0823	0.75394	0.40885
3	0.1235	0.75340	0.42368
4	0.1646	0.75440	0.43104
5	0.2058	0.75497	0.43498
6	0.2469	0.75563	0.43747
7	0.2881	0.75630	0.43917
8	0.3292	0.75696	0.44043
9	0.3704	0.75763	0.43141
10	0.4115	0.75830	0.43220

(b) When $l/b = 0.2$ under $K_{I,\lambda_1} = F_{I,\lambda_1} \sigma' \Big _{\sigma' = 1} \sqrt{\pi l}^{1-\lambda_1} \Big _{l/b = 0.2} = K_{I,\lambda_1}^*$			
$i$	$r/l$	$\sigma_\theta \times r^{1-\lambda_1}$	$\tau_{r\theta} \times r^{1-\lambda_2}$
0	0	0	0
1	0.0206	0.71459	0.29340
2	0.0412	0.75625	0.34544
3	0.0617	0.75543	0.35790
4	0.0823	0.75614	0.36402
5	0.1029	0.75640	0.36726
6	0.1235	0.75673	0.36838
7	0.1440	0.75706	0.37057
8	0.1646	0.75738	0.37150
9	0.1852	0.75770	0.37220
10	0.2050	0.75800	0.37270

The exact stress distributions for  $l/b = 0.1$  are given by substituting the values  $F_I = 1.107$  and  $F_{II} = 0.611$  (see Table 4) into equations (12) and (13); then we have  $\sigma_\theta = 1.207/r^{1-\lambda_1}$  and  $\tau_{r\theta} = 0.820/r^{1-\lambda_2}$ . The FE mesh as shown in Figure 5 cannot provide the exact stress

$\sigma_\theta = 1.207/r^{1-\lambda_1}$  and  $\tau_{r\theta} = 0.820/r^{1-\lambda_2}$  but  $\sigma_\theta = 0.756/r^{1-\lambda_1}$  and  $\tau_{r\theta} = 0.440/r^{1-\lambda_2}$  for  $l/b = 0.1$ ,  $\gamma = 60^\circ$ , and  $\beta = 30^\circ$ . Utilizing this fact, we can obtain accurate results for other geometries. Since FEM error of mixed mode-type ISSF is also controlled by the

**Table 6.** Stress ratio distribution along the notch bisector in Figure 4 when  $\gamma = 60^\circ$  and  $\beta = 30^\circ$ .

$i$	$\sigma_\theta _{l/b=0.1}$	$\tau_{r\theta} _{l/b=0.1}$
	$\sigma_\theta _{l/b=0.2}$	$\tau_{r\theta} _{l/b=0.2}$
0	–	–
1	0.99666	1.18338
2	0.99695	1.18358
3	0.99731	1.18381
4	0.99770	1.18409
5	0.99811	1.18440

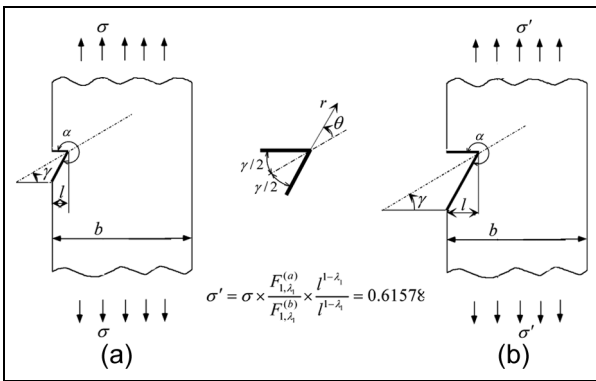


**Figure 4.** Inclined notch  $\gamma = 60^\circ$  and  $\beta = 30^\circ$  in a strip when (a)  $l/b = 0.1$  and (b)  $l/b = 0.2$ .

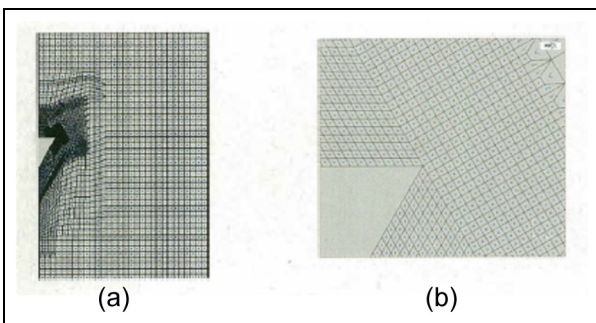


**Figure 5.** Finite element mesh when  $\gamma = 60^\circ$  and  $\beta = 30^\circ$ : (a) mesh of the sharp notch in a strip and (b) mesh around the sharp notch corner.

mesh size around the corner, the error can be eliminated by applying the same mesh pattern to the unknown problem and the reference problem. The detailed discussion has been indicated in Zhang et al.<sup>25</sup> and Noda et al.<sup>26</sup>

From Table 6, it is seen that  $K_{I,\lambda_1}|_{l/b=0.1} \cong K_{I,\lambda_1}|_{l/b=0.2} \cong 0.997$  and  $K_{II,\lambda_2}|_{l/b=0.1} \cong K_{II,\lambda_2}|_{l/b=0.2} \cong 1.184$ . Using these results and exact solution for  $l/b = 0.1$ , the results for  $l/b = 0.2$  are given as shown in Table 7. In Table 7, it is seen that the present method has four-digit accuracy.

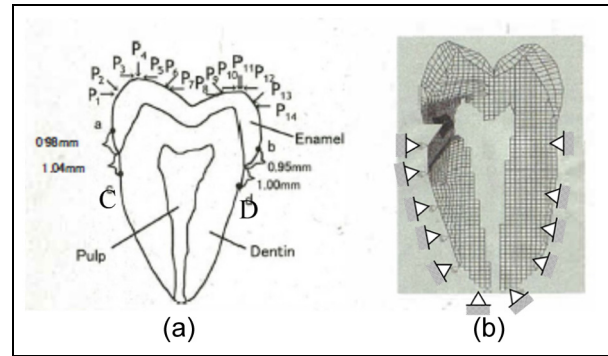


**Figure 6.** Two-dimensional model of human tooth: (a) without wedge-shaped defect with the occlusal force locations and directions  $P_i$  ( $i = 1-14$ ) and (b) with wedge-shaped defect with FEM mesh and fixed displacement boundary conditions.

**Results and discussion**

*Validity of 2D modeling for a maxillary second premolar*

An example of a maxillary second premolar is considered for the wedge-shaped defect as shown in Figure 1. Then a 2D model is constructed with the fixed displacement as shown in Figure 6(b) for the FE analysis. FEM code MARC MENTAT (MSC Software Corporation, 2012) is employed with the four-node quad element. Multi-frontal method is used in the solution of simulation of equations. The total element number is about 223,000. The smallest element size at the end is  $1/3^8 = 0.153 \mu\text{m}$ . Human tooth consists of pulp, enamel, and dentin as shown in Figure 6, and the elastic constants as shown in Table 8<sup>38-40</sup> are assumed neglecting the elastic modulus of pulp. From Table 8, the singular index can be calculated as shown in Table 9 using the eigen equations shown in Appendix 1 as equations (14), (15), (20), (26), and (27) for end A and corner B when  $E_I/E_M = 0, 300/1200, 500/1200, 1000/1200, 2000/1200,$  and  $2500/1200$ . Here,  $E_I$  is the elastic modulus of the composite resin and  $E_M$  is the elastic modulus of the dentin. The FE mesh in Figure 6(b) is the same as the mesh in Figure 5 around the wedge-shaped defect. First, a maxillary second premolar without the defect as shown in Figure 6(a) is analyzed, and the results are compared with the previous study using strain gauge measurement.<sup>6</sup> Here, the strains are measured at four points, namely, (a) the coronal bucco-cervical region, (b) the coronal linguo-cervical region, (c) the root bucco-cervical region, and (d) the root linguo-cervical region when the occlusal forces  $P_2, P_4, P_6, P_9, P_{11},$  and  $P_{13}$  are applied. In previous studies,<sup>6,41</sup> a human maxillary second premolar was used.

Figure 7 shows the comparison between the results of strain gauge and FEM to confirm the validity of 2D model shown in Figure 6. In the experiment,<sup>6</sup> the same maxillary second premolar teeth without the wedge-shaped defect were used and the effects were considered

**Table 7.** Dimensionless ISSFs  $K_{I,\lambda_1}$ ,  $K_{II,\lambda_2}$  defined in equation (11) for the sharp notch in a strip when  $\gamma = 60^\circ$  and  $\beta = 30^\circ$  in Figure 4.

	$l/b$	FEM	BFM	FEM error (%)
$F_{I,\lambda_1}$	0.1	1.107	1.107	0
	0.2	1.282	1.284	0.187
$F_{II,\lambda_2}$	0.1	0.611	0.611	0
	0.2	0.697	0.695	-0.258

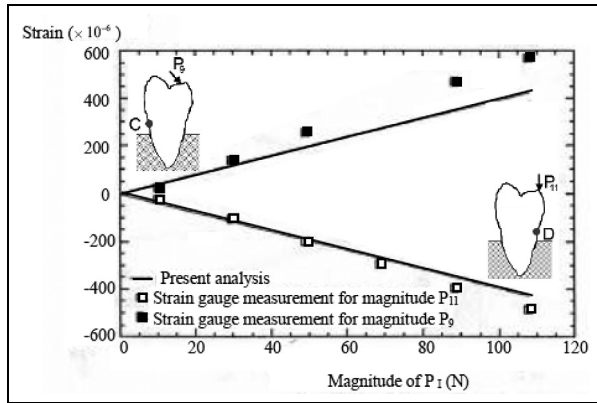
FEM: finite element method; BFM: body force method.

**Table 8.** Mechanical properties for human teeth.<sup>38–40</sup>

Material	Elastic modulus (MPa)	Poisson's ratio	Tensile strength (MPa) (strain $\times 10^{-6}$ )	Compression strength (MPa) (strain $\times 10^{-6}$ )
Pulp	9.81	0.49	–	–
Dentin	11,800	0.30	–	213–380 (1810–32,300)
Enamel	46,100	0.30	10.4–45.6 (226–989)	176–608 (3820–13,200)

**Table 9.** Singular index for the ISSFs defined in equations (10), (17), and (22).

Corners in Figure 1(b)	Singular index	$E_I/E_M$					
		0	300/1200	500/1200	1000/1200	2000/1200	2500/1200
A	$\lambda$	0.7112	0.8878	0.9445	0.9971	0.9788	0.9590
B	$\lambda_1$	0.5122	0.8240	0.9005	0.9834	0.9114	0.8767
	$\lambda_2$	0.7309	0.8593	0.9087	0.9816	1.0000	1.0000

 $E_I$  is the Young's modulus of composite resin;  $E_M$  is the Young's modulus of dentin.**Figure 7.** Strain at points C and D caused by the occlusal forces  $P_6$  and  $P_{11}$  to conform the validity of 2D modeling.

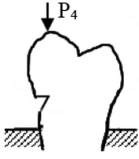
for loads  $P_2$ ,  $P_4$ ,  $P_6$ ,  $P_9$ ,  $P_{11}$ , and  $P_{13}$  in Figure 6. Then the stresses at C and D in Figure 6(a) were compared. As shown in Figure 7, most of the results are in good agreement. However, 4 results of 24 are very different. This is perhaps because of the shape difference between the maxillary second premolar used in those studies. In Figure 7, the experimental and FEM results are compared for the maxillary second premolar without wedge-shaped defect. Since the wedge-shaped defect geometry is 2D as shown in Figure 1, the validity of 2D modeling is confirmed in the above discussion.

### Effect of occlusal force on the ISSF of the wedge-shaped defect before restoration with composite resin

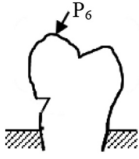
First of all, the ISSF of the wedge-shaped defect is considered before restoration with composite resin. The ISSF is indicated in Appendix 1 as equations (10)–(16). Table 10 indicates the stresses  $\sigma_\theta$ ,  $\tau_{r\theta}$  along the bisector of the wedge-shaped defect. It is seen that the values of  $\sigma_\theta \times r^{1-\lambda_1}$  and  $\tau_{r\theta} \times r^{1-\lambda_2}$  are nearly constant, and therefore, ISSFs can be obtained. It should be noted that the results in Table 10 include some numerical error. However, the error can be eliminated using the exact solution used as the reference problem by applying the same mesh pattern as shown in Tables 2 and 3 with Figure 5. Therefore, the ISSF can be obtained very accurately.

Figure 9 indicates the ISSFs  $F_{\theta B}|_{\theta=0^\circ}$  and  $F_{r\theta B}|_{\theta=0^\circ}$ . Here, the singular stresses along the bisector can be expressed as  $\sigma_\theta|_{\theta=0^\circ} = F_{\theta B}|_{\theta=0^\circ}/r^{1-\lambda_1}$  and  $\tau_{r\theta}|_{\theta=0^\circ} = F_{r\theta B}|_{\theta=0^\circ}/r^{1-\lambda_2}$  (see Appendix 1)

$$\begin{aligned} \sigma_\theta|_{\theta=0^\circ} &= \frac{K_{I,\lambda_1}}{r^{1-\lambda_1}} f_\theta|_{\theta=0^\circ} = \frac{F_{\theta B}|_{\theta=0^\circ}}{r^{1-\lambda_1}}, \\ F_{\theta B}|_{\theta=0^\circ} &= ISSF \\ \tau_{r\theta}|_{\theta=0^\circ} &= \frac{K_{II,\lambda_2}}{r^{1-\lambda_2}} f_\theta|_{\theta=0^\circ} = \frac{F_{r\theta B}|_{\theta=0^\circ}}{r^{1-\lambda_2}}, \\ F_{r\theta B}|_{\theta=0^\circ} &= ISSF \end{aligned} \quad (6)$$

**Table 10.** Stress along the notch bisector in Figure 6(b).


$i$	$\sigma_\theta \times r^{1-\lambda_1}$	$\tau_{r\theta} \times r^{1-\lambda_2}$
(a) $\sigma_\theta, \tau_{r\theta}$ due to $P_4$ ( $r = i/243$ ) (mm)		
0	0	0
1	-0.50344	-0.27129
2	-0.53177	-0.31947
3	-0.53016	-0.33255
4	-0.52965	-0.33707
5	-0.52884	-0.34033
6	-0.52810	-0.34249
7	-0.52737	-0.34406
8	-0.52664	-0.34530
9	-0.52900	-0.34634
10	-0.52516	-0.34727
11	-0.52443	-0.34814
12	-0.52373	-0.34898
13	-0.52323	-0.34974
14	-0.52264	-0.35074
15	-0.52158	-0.35236



$i$	$\sigma_\theta, \tau_{r\theta}$ due to $P_6$ ( $r = i/243$ ) (mm)	
0	0	0
1	-0.70479	-0.52269
2	-0.74451	-0.61527
3	-0.74215	-0.63746
4	-0.74124	-0.64840
5	-0.73984	-0.65422
6	-0.73850	-0.65786
7	-0.73712	-0.66032
8	-0.73572	-0.66213
9	-0.73429	-0.66353
10	-0.73284	-0.66468
11	-0.73139	-0.66567
12	-0.72995	-0.66660
13	-0.72879	-0.66737
14	-0.72752	-0.66860
15	-0.72557	-0.67187

In Figure 8(a), the ratio of the maximum tensile stress and the compressive stress is about 1:1. It is known that the strength ratio of enamel under tension to under compression is 1:10. Therefore, the tensile stress may be more harmful than the compressive stress for enamel.

The compressive strength about dentin is 213–380 MPa. Although there is little study on the tensile strength of dentin, it has been told that it is about 1/7

of the compressive strength. Therefore, the tensile stress may also be more harmful than the compressive stress for dentin.

From Figure 8, it is found that load  $P_{11}$  may be most harmless because of the subtraction of the compressive due to load  $P_{11}$  and the tensile stress due to the bending moment. On the other hand, the occlusal forces  $P_3, P_8, P_{10}$ , and  $P_{12}$  acting on the vertical directions to the tooth axis seem most harmful perhaps because the stress due to the bending moments becomes larger in those occlusal forces. If the occlusion can be adjusted as in the direction of  $P_{11}$ , the risk of extension or fracture from the wedge-shaped defect may be reduced.

### Effect of occlusal force on the ISSF at the interface end A of the wedge-shaped defect after restoration with composite resin

Next, we consider the maxillary second premolar with wedge-shaped defect after restoration by composite resin. Then a 2D FE model in Figure 2(d) is constructed using similar mesh as shown in Figure 6(b). Human tooth model consists of enamel, dentin, and composite resin as shown in Figure 6, and the elastic constants as shown in Table 8 are assumed; however, the elastic modulus of the pulp is neglected.

At the interface end A, a singular stress field appears as shown in equations (17) and (18)<sup>42,43</sup> in Appendix 1. The debonding may be controlled by the interface stress  $\sigma_{\theta A}|_{\theta=90^\circ}$  along  $\theta=90^\circ$  in Figure 9. The intensity of the singular stress  $\sigma_{\theta A}|_{\theta=90^\circ}$  is expressed by the ISSF  $F_{\theta A}|_{\theta=90^\circ}$  as shown in the following equation

$$\begin{aligned} \sigma_{\theta A}|_{\theta=90^\circ} &= \frac{K}{r^{1-\lambda}} f_{\theta}|_{\theta=90^\circ} \\ &= \frac{F_{\theta A}|_{\theta=90^\circ}}{r^{1-\lambda}}, F_{\theta A}|_{\theta=90^\circ} = ISSF \end{aligned} \quad (7)$$

Figure 10 shows the ISSFs  $F_{\theta A}|_{\theta=90^\circ}$  versus  $P_i$  relations when  $E_I/E_M = 300/1200$ . Assume the stress component  $\sigma_\theta$  is most harmful for the debonding at end A. From Figure 10,  $P_{13}$  is most harmless when  $E_I/E_M = 300/1200$ . Similar results are obtained when  $E_I/E_M = 500/1200$  and  $1000/1200$ . Figure 11 shows the ISSF  $F_{\theta A}|_{\theta=90^\circ}$  at end A versus  $P_i$  relations when  $E_I/E_M = 2000/1200$ . From Figure 11,  $P_2$  is most harmless when  $E_I/E_M = 2000/1200$ . Similar results are obtained when  $E_I/E_M = 2500/1200$ . The most harmless load is depending on the ratio  $E_I/E_M$ . On the other hand, the harmful occlusal forces are  $P_1, P_3, P_8$ , and  $P_{10}$  and the most harmful load is always  $P_3$ .

### Effect of occlusal force on the ISSF at corner B of the wedge-shaped defect after restoration with composite resin

For corner B, the singular stress should be considered depending on  $E_I/E_M$ . They are expressed in equations (22)–(32)<sup>44</sup> in Appendix 1. When  $E_I/E_M < 1$ , the stress

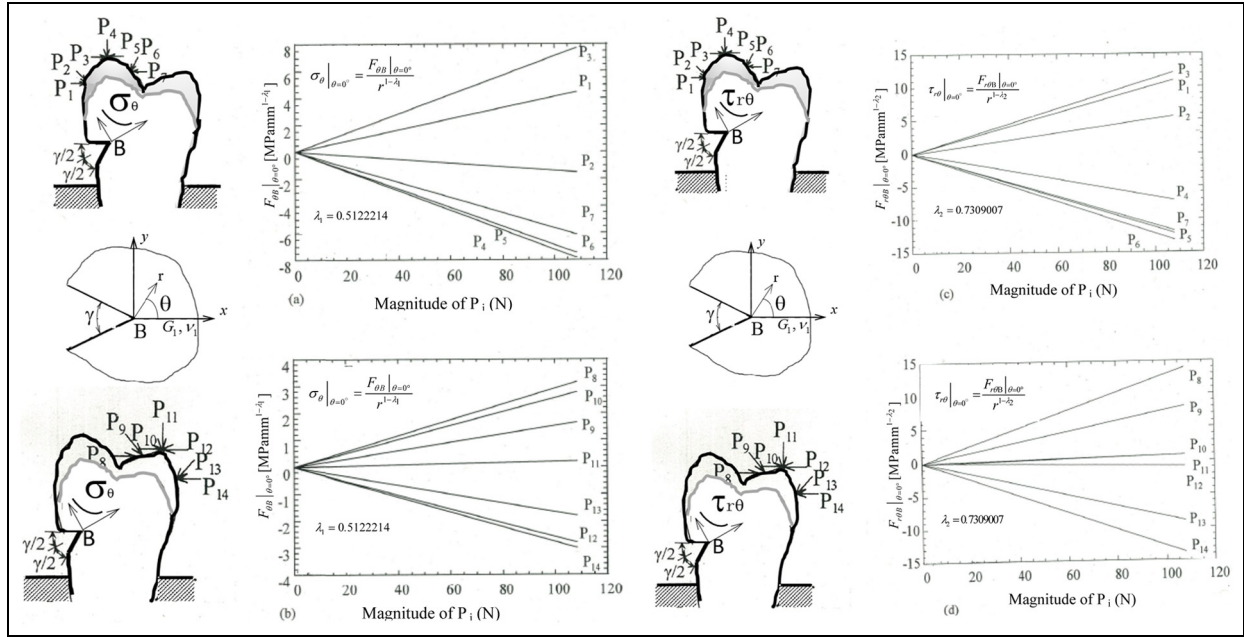


**Figure 8.** ISSFs at corner B defined in equation (16) due to the occlusal forces  $P_i$  (a), (c)  $P_1$ – $P_7$  are applied to the buccal side of the teeth (b), and (d)  $P_8$ – $P_{14}$  are applied to the lingual side of the teeth. ISSF: intensity of singular stress field.

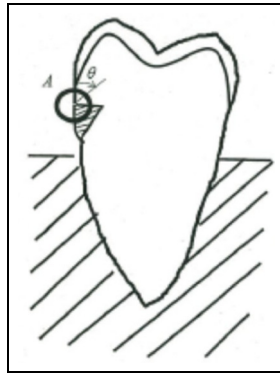


**Figure 9.** Singular stress field for the interface end A.

along the bisector  $\theta = 0^\circ$  in Figure 12 is most harmful, and it can be expressed in equation (22) in Appendix 1.

When  $E_I < E_M$ , the stress along the bisector  $\sigma_{\theta B}|_{\theta=0^\circ}$  should be considered (see Appendix 1)

$$\begin{aligned} \sigma_{\theta B}|_{\theta=0^\circ} &= \frac{K_{I,\lambda_1}}{r^{1-\lambda_1}} f_\theta^I(\theta)|_{\theta=0^\circ} \\ &= \frac{F_{\theta B}|_{\theta=0^\circ}}{r^{1-\lambda_1}}, F_{\theta B}|_{\theta=0^\circ} = ISSF \end{aligned} \quad (8)$$

Figure 13 shows the ISSF  $F_{\theta B}|_{\theta=0^\circ}$  and versus  $P_i$  ( $i = 1-14$ ) relations when  $E_I/E_M = 300/1200$ . In Figure 13, it is known that the tensile and compressive strength of enamel are in the ratio of 1:10 (see Table 8). Therefore, the tensile stress may be more harmful than the compressive stress for enamel. The compressive strength about dentin is 213–380 MPa. Since the tensile strength of the dentin is about 1/7 of the compressive

strength, the tensile stress may also be more harmful than compressive stress for the dentin. From Figure 13, it is found that load  $P_9$  may be most harmless because the compressive due to loads  $P_9$  and  $P_{11}$  and the tensile stress due to the bending moment may cancel each other. On the other hand, the occlusal forces  $P_1$ ,  $P_3$ ,  $P_8$ , and  $P_{10}$  acting in perpendicular to the tooth axis are most harmful perhaps because the stress due to the bending moments becomes larger in those occlusal forces. Similar results were obtained when  $E_I/E_M = 500/1200$  and  $1000/1200$ . If the occlusion can be adjusted as in the direction of  $P_{11}$ , the risk of fracture from the wedge-shaped defect may be reduced.

On the other hand, when  $E_I/E_M > 1$  the debonding should be considered along the interface, that is,  $\theta \pm 150^\circ$  in Figures 12 and 13. When  $E_I/E_M = 2000/1200$  and  $2500/1200$ , the singular index  $\lambda_2 = 1.0$ , and therefore, no mode II singular stress. Then the singular stress field is expressed in equation (9) by  $K_{I,\lambda_1}$  alone.

When  $E_I > E_M$ , the interface stress  $\sigma_{\theta B}|_{\theta=\pm 150^\circ}$  should be considered (see Appendix 1)

$$\begin{aligned} \sigma_{\theta B}|_{\theta=\pm 150^\circ} &= \frac{K_{I,\lambda_1}}{r^{1-\lambda_1}} f_\theta^I(\theta)|_{\theta=150^\circ} \\ &= \frac{F_{\theta B}^I|_{\theta=150^\circ}}{r^{1-\lambda_1}}, F_{\theta B}^I|_{\theta=150^\circ} \\ &= K_{I,\lambda_1} f_\theta^I(\theta)|_{\theta=150^\circ} = ISSF \end{aligned} \quad (9)$$

Assume the ISSF  $F_{\theta B}^I|_{\theta=150^\circ}$  is the most harmful for the fracture at the corner of wedge-shaped inclusion. Figure 14 shows the ISSF  $F_{\theta B}^I|_{\theta=150^\circ}$  at corner B versus  $P_i$  relations when  $E_I/E_M = 2000/1200$ . As shown in Figure 14, it is found that the occlusal force  $P_{11}$  may be

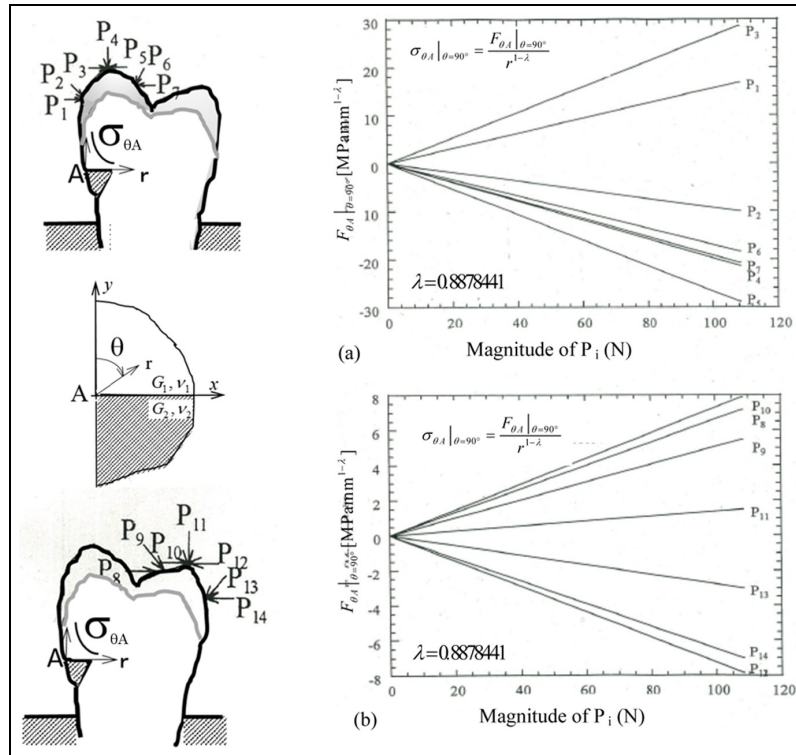


**Figure 10.** ISSFs at end A defined in equation (21) due to occlusal forces  $P_i$  when  $E_I/E_M = 300/1200$ : (a)  $P_1$ – $P_7$  are applied to the buccal side of the teeth and (b)  $P_8$ – $P_{14}$  are applied to the lingual side of the teeth. ISSF: intensity of singular stress field.

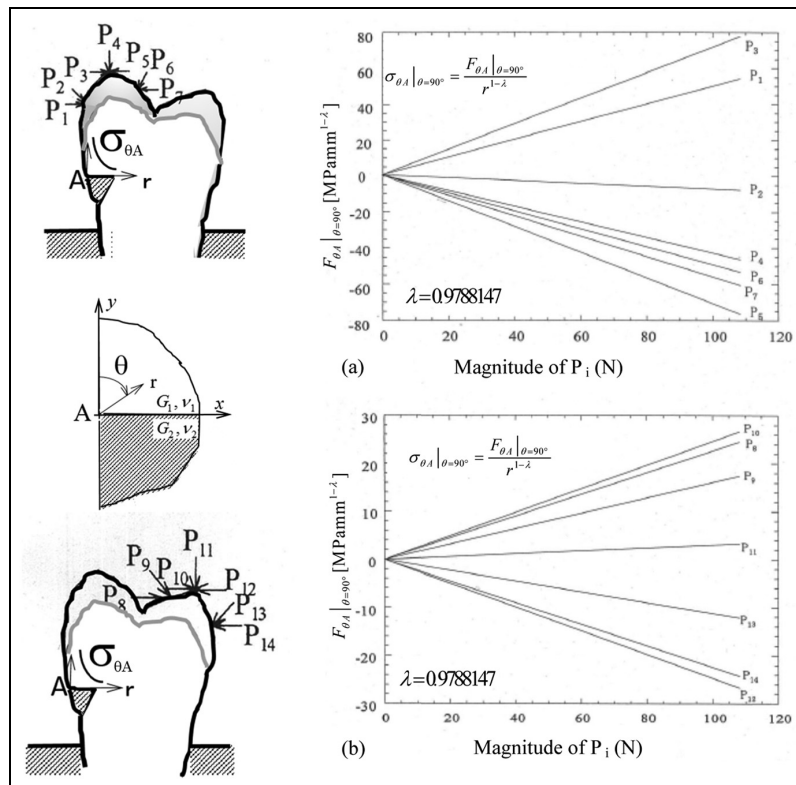


**Figure 11.** ISSFs at the interface end A defined in equation (21) due to occlusal forces  $P_i$  when  $E_I/E_M = 2000/1200$ : (a)  $P_1$ – $P_7$  are applied to the buccal side of the teeth and (b)  $P_8$ – $P_{14}$  are applied to the lingual side of the teeth. ISSF: intensity of singular stress field.

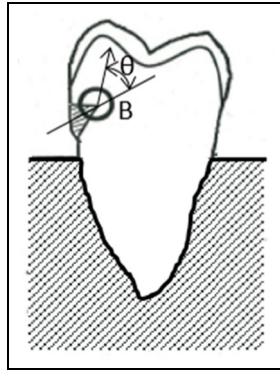


**Figure 12.** Singular stress field for corner B.

most harmless. On the other hand, the occlusal forces  $P_1, P_3, P_8,$  and  $P_{10}$  are harmful because they cause tensile stresses at the interface. Similar results are obtained when  $E_I/E_M = 2500/1200$ . If the occlusion can be adjusted as in the direction of  $P_{11}$ , the risk of fracture may be reduced.

**Conclusion**

Wedge-shaped defects are frequently observed on the cervical region of the human tooth. Previously, most studies explained that improper tooth-brushing causes such defects. However, recent clinical observation

suggested that the repeated stress due to occlusal force may induce the formation of these wedge-shaped defects. In this study, 2D human tooth models were considered with and without a wedge-shaped defect by applying the FEM. Then the relationship between the stress intensity and occlusion was discussed before and after restoration with composite resins. The conclusions can be summarized in the following way:

1. As shown in Figure 6, the intensity of the singular stress was investigated with varying the position and direction of the occlusal force. It is found that the occlusal force  $P_{11}$  may be most harmless, but the occlusal forces  $P_3, P_8, P_{10},$  and  $P_{12}$  acting in perpendicular directions to the tooth axis seem most harmful. If the occlusion can be adjusted as in the direction of  $P_{11}$ , the risk of extension or fracture from the wedge-shaped defect may be reduced.
2. It was found that the maximum tensile and compressive strain are in the ratio of about 1:3 (see Table 8). Since the tensile and compressive strength of enamel are in the ratio of 1:10, the tensile stress may be more harmful than compressive stress for enamel. Also, since the tensile and compressive strengths of dentin are in the ratio of about 1:7, the tensile stress may also be more harmful than compressive stress for dentin.

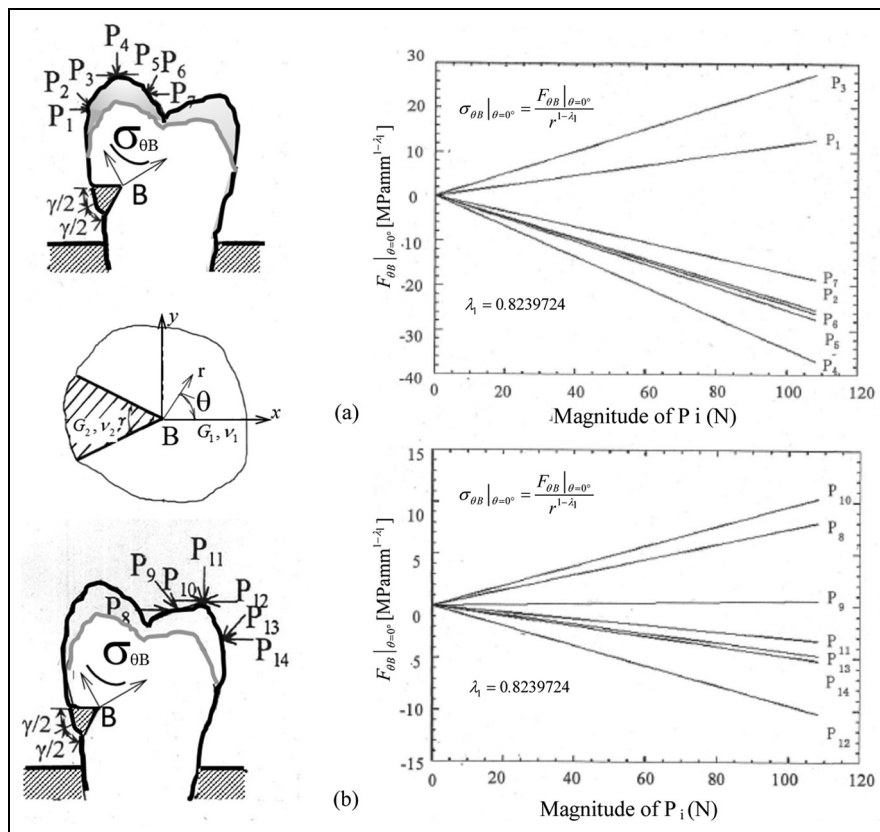


**Figure 13.** ISSFs at corner B defined in equation (29) due to occlusal forces  $P_i$  when  $E_I/E_M = 300/1200$ : (a)  $P_1$ – $P_7$  are applied to the buccal side of the teeth and (b)  $P_8$ – $P_{14}$  are applied to the lingual side of the teeth. ISSF: intensity of singular stress field.

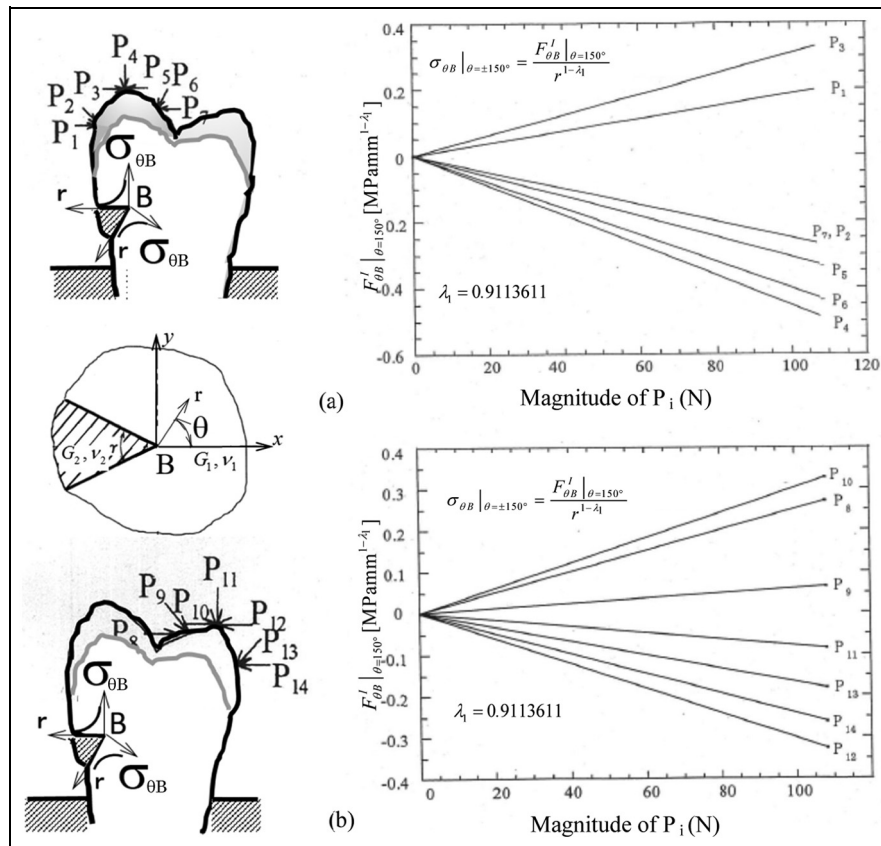


**Figure 14.** ISSFs at corner B defined in equation (30) due to occlusal forces  $P_i$  when  $E_I/E_M = 2000/1200$ : (a)  $P_1$ – $P_7$  are applied to the buccal side of the teeth and (b)  $P_8$ – $P_{14}$  are applied to the lingual side of the teeth. ISSF: intensity of singular stress field.

- The intensity of the singular stress at end A was investigated with varying the position and direction of the occlusal force. As shown in Figures 10 and 11, it is found that  $P_3$  is the most harmful occlusal force for any composite resin and dentin ratio  $E_I/E_M$ . However, occlusal forces  $P_2$ ,  $P_{11}$ , and  $P_{13}$  are the most harmless occlusal force for corner B under different  $E_I/E_M$  ratios, respectively.
- The intensity of the singular stress at corner B was investigated with varying the position and direction of the occlusal force. As shown in Figures 13 and 14, it is found that  $P_3$  is the most harmful occlusal force for any composite resin and dentin ratio  $E_I/E_M$ . However, occlusal forces  $P_9$  and  $P_{11}$  are the most harmless occlusal force for corner B under different  $E_I/E_M$  ratios, respectively.

### Acknowledgements

The authors wish to express their thanks to the members of their group: Mr Shinji Kataoka, Yuichi Nishikore, Ms Hiromi Imoto, Mr Takuya Tsutsumi, and Mr Kyouusuke Yamaguchi, for their constructional works of FEM analysis and preparing the results. The authors also greatly appreciate Professor Hiroyuki Tanaka with Kyushu Institute of Technology, who gave a lot of useful help and advice.

### Declaration of conflicting interests

The author(s) declared no potential conflicts of interest with respect to the research, authorship, and/or publication of this article.

### Funding

The author(s) disclosed receipt of the following financial support for the research, authorship, and/or publication of this article: The research for this article was financially supported by the Japanese Ministry of Education research (grant no. 19560094).

### References

- Miller WD. Experiments and observations on the wasting of tooth tissue variously designated as erosion, abrasion, chemical abrasion, denudation: etc. *Dent Cosm* 1907; 49: 1–23.
- Bream M, Lambrechts P and Vanherle G. Stress-induced cervical lesions. *J Prosthet Dent* 1992; 67: 718–722.
- Graehn G and Muller HH. Wedge-shaped defects of teeth of animals. *Dtsch Zahn Mund Kieferheilkd Zentralbl* 1991; 79: 441–449.
- Tanaka H, Maeda T, Nitta T, et al. Studies on the cervical loss of tooth structure—Japanese teeth before and during the Edo era: the first report Edo era. *Jpn J Conserv Dent* 1993; 36: 287–294.

5. Lee WC and Eakle WS. Possible role of tensile stress in the etiology of cervical lesions of teeth. *J Prosthet Dent* 1984; 52: 374–380.
6. Chen KK, Miyake K, Shono Y, et al. Effects of occlusion on the formation of wedge-shaped defect-cervical region strain along tooth axis. *Jpn J Conserv Dent* 2000; 43: 870–876 (in Japanese).
7. Anan K. Potential of stress-inducing wedge-shaped defect of tooth. *Kyushu Dent Soc* 1996; 50: 307–318 (in Japanese).
8. Kuroe T, Caputo A, Ohara AN, et al. Biomechanics of cervical tooth structure lesions and their restoration. *Quintessence Int* 2000; 34: 267–274.
9. Kuroe T, Caputo A, Ohara AN, et al. Biomechanical effects of cervical lesions and restoration on periodontally compromised teeth. *Quintessence Int* 2001; 20: 1501–1510 (in Japanese).
10. Imbeni V, Nalla RK, Bosi C, et al. In vitro fracture toughness of human dentin. *J Biomed Mater Res A* 2003; 66: 1–9.
11. Imbeni V, Kruzic JJ, Marshall GW, et al. The dentin-enamel junction and the fracture of human teeth. *Nat Mater* 2005; 4: 229–232.
12. Yahyazadehfer M, Ivancik J, Majd H, et al. On the mechanics of fatigue and fracture in teeth. *Appl Mech Rev* 2014; 66: 0308031–3080319.
13. Brian RL, Herzl C, Amir B, et al. Transverse fracture of canine teeth. *J Biomech* 2013; 46: 1561–1567.
14. Cernescu A, Faur N, Bortun C, et al. A methodology for fracture strength evaluation of complete denture. *Eng Fail Anal* 2011; 18: 1253–1261.
15. Sabine B, Theo F, Gabriele R, et al. Crack arrest within teeth at the dentinoenamel junction caused by elastic modulus mismatch. *Biomaterials* 2010; 31: 4238–4247.
16. Ritchie RO, Kinney JH, Kruzic JJ, et al. A fracture mechanics and mechanistic approach to the failure of cortical bone. *Fatigue Fract Eng Mat Struct* 2005; 28: 345–371.
17. Nalla RK, Kruzic JJ, Kinney JH, et al. Mechanistic aspects of fracture and R-curve behavior in human cortical bone. *Biomaterials* 2005; 26: 217–231.
18. Vashishth D, Behiri JC and Bonfield W. Crack growth resistance in cortical bone: concept of microcrack toughening. *J Biomech* 1997; 30: 763–769.
19. Nalla RK, Kruzic JJ and Ritchie RO. On the origin of the toughness of mineralized tissue: microcracking or crack bridging? *Bone* 2004; 34: 790–798.
20. Nalla RK, Kruzic JJ, Kinney JH, et al. Effect of aging on the toughness of human cortical bone: evaluation by R-curves. *Bone* 2004; 35: 1240–1246.
21. Wu PC and Vashishth D. Age related changes in cortical bone toughness. In: *Proceedings of the 2nd joint EMBS/BMES conference*, Houston, TX, 23–26 October 2002, pp. 425–426. New York: IEEE.
22. Katharina Z, Elke V, Uwe G, et al. Reinforcement of a magnesium-ammonium-phosphate cement with calcium phosphate whiskers. *J Am Ceram Soc* 2015; 98: 4028–4035.
23. Logan S, Tuslt W, Allan G, et al. Rate-dependent fracture modes in human femoral cortical bone. *Int J Fracture* 2015; 194: 81–92.
24. Bouziane MM, Bachir Bouiadjra B, Benbarek S, et al. Analysis of the behavior of cracks emanating from bone inclusion and ordinary cracks in the cement mantle of total hip prosthesis. *J Braz Soc Mech Sci* 2015; 37: 11–19.
25. Zhang Y, Noda N-A, Wu P, et al. Corrigendum to “A mesh-independent technique to evaluate stress singularities in adhesive joints.” *Int J Adhes Adhes* 2015; 57: 105–117.
26. Noda N-A, Miyazaki T, Li R, et al. Debonding strength evaluation in terms of the intensity of singular stress at the interface corner with and without fictitious crack. *Int J Adhes Adhes* 2015; 61: 46–64.
27. Chen DH and Nisitani H. Stress intensity factors of a strip with a v-shaped single notch under tension or in-plane bending. *Trans JSME* 1993; 59: 187–192 (in Japanese).
28. Noda N-A, Wang Q, Takase Y, et al. Intensity of singular stress field at the notch tip of a V-notched bar. *Trans JSME* 1999; 65: 2299–2302 (in Japanese).
29. Noda N-A and Takase Y. Generalized stress intensity factors of V-shaped notch in a round bar under torsion, tension, and bending. *Eng Fract Mech* 2003; 70: 1447–1466.
30. Noda N-A, Kawashima Y, Moriyama S, et al. Interaction of newly defined stress intensity factors for angular corners in a row of diamond-shaped inclusions. *Int J Fracture* 1996; 82: 267–295.
31. Yamaguchi K, Noda N-A, Chen K-K, et al. Generalized stress intensity factor for wedge-shaped defect in human tooth after restored with composite resins. *Struct Durab Health Mon* 2009; 5: 191–199.
32. Nisitani H. The two-dimensional stress problem solved using an electric digital computer (also published in *Bull JSME* 1968; 11: 14–23). *Trans JSME* 1967; 11: 627–632 (in Japanese).
33. Nisitani H. Solution of notch problems by body force method. In: Sih GC (ed.) *Mechanics of fracture*. Leuden: Noodhoff, 1978, p. 5.
34. Noda N-A and Matsuo T. Singular integral equation method for interaction between elliptical inclusions: *J Appl Mech: T ASME* 1998; 65: 310–319.
35. Noda N-A and Moriyama Y. Stress concentration of an ellipsoidal inclusion of revolution in a semi-infinite body. *Arch Appl Mech* 2004; 74: 29–44.
36. Teranishi T and Nisitani H. Determination of highly accurate values of stress intensity factor in a plate of arbitrary form by FEM. *Trans JSME* 1999; 65: 16–21 (in Japanese).
37. Nisitani H, Teranishi T and Fukuyama K. Stress intensity factor analysis of a biomaterial plate based on the crack tip stress method. *Trans JSME* 2003; 69: 1203–1208 (in Japanese).
38. Tajima K, Chen KK, Yokoyama Y, et al. Numerical analysis of stress in enamel induced by polymerization shrinkage of composite resin for class v restorations. *Kyushu Dent Soc* 1992; 46: 389–397 (in Japanese).
39. Okazaki K, Nishimura F, Nomoto S, et al. Tensile strength of human enamel. *Dent Mater* 1987; 6: 465–471 (in Japanese).
40. Nishimura F, Okazaki K, Kono Y, et al. Compressive behavior and micro Vickers hardness of human enamel and dentin. *Dent Mater* 1986; 5: 449–454. (in Japanese).
41. Noda N-A, Chen KK, Tajima K, et al. Intensity of singular stress of wedge-shaped defect in human tooth due to occlusal load. *Trans JSME* 2006; 72: 77–84 (in Japanese).

42. Chen DH and Nisitani H. Intensity of singular stress field near the interface edge point of a bonded strip. *Trans JSME* 1993; 59: 210–214 (in Japanese).
43. Noda N-A, Shirao R, Li J, et al. Intensity of singular stress fields causing interfacial debonding at the end of a fiber under pullout force and transverse tension. *Int J Solids Struct* 2007; 44: 4472–4491.
44. Noda N-A, Kawashima Y, Moriyama S, et al. Interaction of newly defined stress intensity factors for angular corners in a row of diamond-shaped inclusions. *Int J Fracture* 1996; 82: 267–295.

## Appendix I

### ISSFs considered in this article

In this article, several types of singular stress fields are considered at the corner and interface end, and their ISSFs are discussed. They are indicated in the following way.

*The ISSF of the wedge-shaped defect before restoration with composite resin.* The stress field around the apex of the wedge-shaped defect can be expressed in the following equations

$$\sigma_{ij} = \frac{K_{I,\lambda_1}}{r^{1-\lambda_1}} f_{ij}^I(\theta) + \frac{K_{II,\lambda_2}}{r^{1-\lambda_2}} f_{ij}^{II}(\theta), \quad K_{I,\lambda_1}, K_{II,\lambda_2} = ISSFs \quad (10)$$

$$K_{I,\lambda_1} = F_{I,\lambda_1} \sigma \sqrt{\pi l}^{1-\lambda_1}, \quad K_{II,\lambda_2} = F_{II,\lambda_2} \sigma \sqrt{\pi l}^{1-\lambda_2}, \quad (11)$$

$F_{I,\lambda_1}, F_{II,\lambda_2} = \text{Dimensionless ISSFs}$

For example,  $\sigma_\theta$  and  $\tau_{r\theta}$  are expressed as

$$\begin{aligned} \sigma_\theta = & \frac{\lambda}{\sqrt{2\pi}} [(\lambda_1 + 1) \sin\{\lambda_1(\alpha - \pi)\} \cos(\lambda_1 - 1)\theta \\ & + [\lambda_1 \sin\{\alpha - \lambda_1(\alpha - \pi)\} \\ & + \sin(\lambda_1\pi)] \cos(\lambda_1 + 1)\theta] \frac{K_{I,\lambda_1}}{r^{1-\lambda_1}} \\ & + \frac{\lambda_2}{\sqrt{2\pi}} [(\lambda_2 + 1) \sin\{\lambda_2(\alpha - \pi)\} \sin(\lambda_2 - 1)\theta \\ & + [\lambda_2 \sin\{\alpha - \lambda_2(\alpha - \pi)\} \\ & + \sin(\lambda_2\pi)] \sin(\lambda_2 + 1)\theta] \frac{K_{II,\lambda_2}}{r^{1-\lambda_2}} \end{aligned} \quad (12)$$

$$\begin{aligned} \tau_{r\theta} = & \frac{\lambda_1}{\sqrt{2\pi}} [(\lambda_1 + 1) \sin\{\lambda_1(\alpha - \pi)\} \sin(\lambda_1 - 1)\theta \\ & + [\lambda_1 \sin\{\alpha - \lambda_1(\alpha - \pi)\} \\ & + \sin(\lambda_1\pi)] \sin(\lambda_1 + 1)\theta] \frac{K_{I,\lambda_1}}{r^{1-\lambda_1}} \\ & - \frac{\lambda_2}{\sqrt{2\pi}} [(\lambda_2 - 1) \sin\{\lambda_2(\alpha - \pi)\} \cos(\lambda_2 - 1)\theta \\ & + [\lambda_2 \sin\{\alpha - \lambda_2(\alpha - \pi)\} \\ & - \sin(\lambda_2\pi)] \cos(\lambda_2 + 1)\theta] \frac{K_{II,\lambda_2}}{r^{1-\lambda_2}} \end{aligned} \quad (13)$$

The singular index can be determined from the following characteristic equations:

For mode I

$$\sin\{\lambda_1(2\pi - \gamma)\} = -\lambda_1 \sin \gamma \quad (14)$$

For mode II

$$\sin\{\lambda_2(2\pi - \gamma)\} = \lambda_2 \sin \gamma \quad (15)$$

$$\sigma_\theta = \frac{K_{I,\lambda_1}}{r^{1-\lambda_1}} f_\theta|_{\theta=0^\circ} = \frac{F_{\theta B}|_{\theta=0^\circ}}{r^{1-\lambda_1}}, \quad F_{\theta B}|_{\theta=0^\circ} = ISSF$$

$$\tau_{r\theta} = \frac{K_{II,\lambda_2}}{r^{1-\lambda_2}} f_\theta|_{\theta=0^\circ} = \frac{F_{r\theta B}|_{\theta=0^\circ}}{r^{1-\lambda_2}}, \quad F_{r\theta B}|_{\theta=0^\circ} = ISSF \quad (16)$$

*The ISSF at the interface end A of the wedge-shaped defect after restoration with composite resin.* The singular stress field at the interface end A can be expressed in the following equations<sup>42,43</sup>

$$\sigma_{\theta A} = \frac{K}{r^{1-\lambda}} f_\theta(\theta), \quad \tau_{r\theta} = \frac{K}{r^{1-\lambda}} f_{r\theta}(\theta), \quad K = ISSF \quad (17)$$

$$f_\theta(\theta) = m_1 \cos\{(\lambda - 1)\theta\} - m_2 \sin\{(\lambda - 1)\theta\} \\ - m_1 \cos\{(\lambda + 1)\theta\} + m_3 \sin\{(\lambda + 1)\theta\}$$

$$f_{r\theta}(\theta) = m_3 \cos\{(\lambda - 1)\theta\} + m_4 \sin\{(\lambda - 1)\theta\} \\ - m_3 \cos\{(\lambda + 1)\theta\} - m_1 \sin\{(\lambda + 1)\theta\}$$

$$m_1 = \lambda(\lambda + 1) Y_2, \quad m_2 = \lambda(\lambda + 1) Y_1,$$

$$m_3 = \lambda(\lambda - 1) Y_1, \quad m_4 = \lambda(\lambda - 1) Y_2 \quad (18)$$

$$Y_1 = 4\lambda\beta \cos(\lambda\pi) + 2\beta[\cos(\lambda\pi) - 1] + 4\lambda(\lambda + 1)(\alpha - \beta)$$

$$Y_2 = 2(2\lambda\beta - 1) \sin(\lambda\pi), \quad Y_3 = -Y_1,$$

$$Y_4 = -2(2\lambda\beta + 1) \sin(\lambda\pi)$$

$$L_1 = 2\lambda \cos(\lambda\pi/2) Y_4 - 2(\lambda - 1) \sin(\lambda\pi/2) Y_3$$

$$L_2 = -2\lambda \cos(\lambda\pi/2) Y_2 + 2(\lambda - 1) \sin(\lambda\pi/2) Y_1 \quad (19)$$

The singular index can be determined from the following characteristic equation (Figure 15)

$$\begin{aligned} & \left[ \sin^2\left(\frac{\pi}{2}\lambda\right) - \lambda^2 \right]^2 \beta^2 + 2\lambda^2 \left[ \sin^2\left(\frac{\pi}{2}\lambda\right) - \lambda^2 \right] \\ & \alpha\beta + \lambda^2(\lambda^2 - 1)\alpha^2 + \frac{\sin^2(\pi\lambda)}{4} \end{aligned} \quad (20)$$

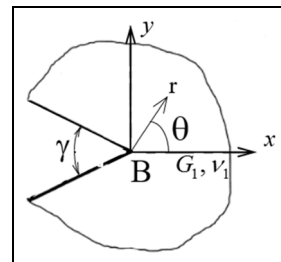
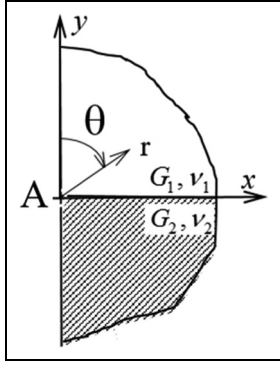
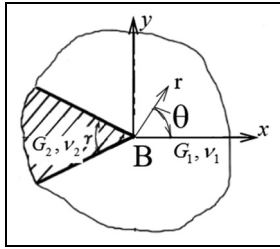


Figure 15. Sharp notch..



**Figure 16.** Interface end A.



**Figure 17.** V-shaped inclusion corner B.

The debonding may be controlled by the interface stress  $\sigma_{\theta A}|_{\theta=90^\circ}$  along  $\theta=90^\circ$  in Figure 16. The intensity of the interface singular stress field is expressed by the ISSF  $F_{\theta A}|_{\theta=0^\circ}$  as shown in the following equation

$$\sigma_{\theta A}|_{\theta=90^\circ} = \frac{K}{r^{1-\lambda}} f_{\theta}|_{\theta=90^\circ} = \frac{F_{\theta A}|_{\theta=90^\circ}}{r^{1-\lambda}}, \quad (21)$$

$$F_{\theta A}|_{\theta=90^\circ} = K f_{\theta}|_{\theta=90^\circ} = ISSF$$

The ISSF at corner B of the wedge-shaped defect after restoration with composite resin. The singular stress field at corner B can be expressed in the following equations (Figure 17)

$$\sigma_{ij} = \frac{K_{I\lambda_1}}{r^{1-\lambda_1}} f_{ij}^I(\theta) + \frac{K_{II\lambda_2}}{r^{1-\lambda_2}} f_{ij}^{II}(\theta), K_{I\lambda_1}, K_{II\lambda_2} = ISSFs \quad (22)$$

$$K_{I\lambda_1} = F_{I\lambda_1} \sigma \sqrt{\pi} l^{1-\lambda_1}, K_{II\lambda_2} = F_{II\lambda_2} \sigma \sqrt{\pi} l^{1-\lambda_2}, \quad (23)$$

$$F_{I\lambda_1}, F_{II\lambda_2} = \text{Dimensionless ISSF}$$

$$\sigma_{\theta} = \frac{\lambda_1}{\sqrt{2\pi}(\alpha - \beta)} [[\lambda_1(\alpha - \beta) \sin\{\gamma - \lambda_1(\gamma - \pi)\}]$$

$$+ (1 - \beta) \sin(\lambda_1\pi)] \times \cos\{(\lambda_1 + 1)\theta\} + [(\lambda_1 + 1)$$

$$\times (\alpha - \beta) \sin\{\lambda_1(\gamma - \pi)\}] \times \cos\{(\lambda_1 - 1)\theta\} \frac{K_{I\lambda_1}}{r^{1-\lambda_1}}$$

$$+ \frac{\lambda_2}{\sqrt{2\pi}(\alpha - \beta)} [[\lambda_2(\alpha - \beta) \sin\{\gamma - \lambda_2(\gamma - \pi)\}]$$

$$- (1 - \beta) \sin(\lambda_2\pi)] \times \sin\{(\lambda_2 + 1)\theta\} + [(\lambda_2 + 1)$$

$$\times (\alpha - \beta) \sin\{\lambda_2(\gamma - \pi)\}] \times \sin\{(\lambda_2 - 1)\theta\} \frac{K_{II\lambda_2}}{r^{1-\lambda_2}} \quad (24)$$

$$\tau_{r\theta} = \frac{\lambda_1}{\sqrt{2\pi}(\alpha - \beta)} [[\lambda_1(\alpha - \beta) \sin\{\gamma - \lambda_1(\gamma - \pi)\}]$$

$$+ (1 - \beta) \sin(\lambda_1\pi)] \times \sin\{(\lambda_1 + 1)\theta\} + [(\lambda_1 - 1)$$

$$\times (\alpha - \beta) \sin\{\lambda_1(\gamma - \pi)\}] \times \sin\{(\lambda_1 - 1)\theta\} \frac{K_{I\lambda_1}}{r^{1-\lambda_1}}$$

$$+ \frac{-\lambda_2}{\sqrt{2\pi}(\alpha - \beta)} [[\lambda_2(\alpha - \beta) \sin\{\gamma - \lambda_2(\gamma - \pi)\}]$$

$$- (1 - \beta) \sin(\lambda_2\pi)] \times \cos\{(\lambda_2 + 1)\theta\} + [(\lambda_2 - 1)$$

$$\times (\alpha - \beta) \sin\{\lambda_2(\gamma - \pi)\}] \times \cos\{(\lambda_2 - 1)\theta\} \frac{K_{II\lambda_2}}{r^{1-\lambda_2}} \quad (25)$$

The singular index can be determined from the following characteristic equations:

For mode I

$$(\alpha - \beta)^2 \lambda_1^2 (1 - \cos 2\gamma) + 2\lambda_1(\alpha - \beta) \sin \gamma$$

$$\times \{\sin \lambda_1 \gamma + \sin \lambda_1(2\pi - \gamma)\}$$

$$+ 2\lambda_1(\alpha - \beta)\beta \sin \gamma \quad (26)$$

$$\times \{\sin \lambda_1(2\pi - \gamma) - \sin \lambda_1 \gamma\}$$

$$+ (1 - \alpha^2) - (1 - \beta^2) \cos 2\lambda_1 \pi$$

$$+ (\alpha^2 - \beta^2) \cos\{2\lambda_1(\gamma - \pi)\} = 0$$

For mode II

$$(\alpha - \beta)^2 \lambda_2^2 (1 - \cos 2\gamma) - 2\lambda_2(\alpha - \beta) \sin \gamma$$

$$\times \{\sin \lambda_2 \gamma + \sin \lambda_2(2\pi - \gamma)\} - 2\lambda_2(\alpha - \beta)\beta \sin \gamma$$

$$\times \{\sin \lambda_2(2\pi - \gamma) - \sin \lambda_2 \gamma\}$$

$$+ (1 - \alpha^2) - (1 - \beta^2) \cos 2\lambda_2 \pi$$

$$+ (\alpha^2 - \beta^2) \cos\{2\lambda_2(\gamma - \pi)\} = 0 \quad (27)$$

$$\alpha = \frac{G_M(\kappa_I + 1) - G_I(\kappa_M + 1)}{G_M(\kappa_I + 1) + G_I(\kappa_M + 1)}, \kappa_I = 3 - 4\nu_I$$

$$\beta = \frac{G_M(\kappa_I - 1) - G_I(\kappa_M - 1)}{G_M(\kappa_I + 1) + G_I(\kappa_M + 1)}, \kappa_M = 3 - 4\nu_M \quad (28)$$

When  $E_I > E_M$ , the stresses along the bisector  $\sigma_{\theta}|_{\theta=0^\circ}$  and  $\tau_{r\theta}|_{\theta=0^\circ}$  should be considered since the fracture may occur along the bisector

$$\sigma_{\theta B}|_{\theta=0^\circ} = \frac{K_{I\lambda_1}}{r^{1-\lambda_1}} f_{\theta}^I(\theta)|_{\theta=0^\circ} = \frac{F_{\theta B}|_{\theta=0^\circ}}{r^{1-\lambda_1}}, F_{\theta B}|_{\theta=0^\circ}$$

$$= K_{I\lambda_1} f_{\theta}^I(\theta)|_{\theta=0^\circ} = ISSF$$

$$\tau_{r\theta B}|_{\theta=0^\circ} = \frac{K_{II\lambda_2}}{r^{1-\lambda_2}} f_{\theta}^{II}(\theta)|_{\theta=0^\circ}$$

$$= \frac{F_{r\theta B}|_{\theta=0^\circ}}{r^{1-\lambda_2}}, F_{r\theta B}|_{\theta=0^\circ} = K_{II\lambda_2} f_{\theta}^{II}(\theta)|_{\theta=0^\circ} = ISSF \quad (29)$$

When  $E_I > E_M$ , the interface stresses  $\sigma_\theta|_{\theta = \pm 150^\circ}$  and  $\tau_\theta|_{\theta = \pm 150^\circ}$  should be considered since the fracture may occur along the interface

$$\sigma_{\theta B}|_{\theta = 150^\circ} = \frac{F_{\theta B}^I|_{\theta = 150^\circ}}{r^{1-\lambda_1}} + \frac{F_{\theta B}^{II}|_{\theta = 150^\circ}}{r^{1-\lambda_2}} \quad (30)$$

$$F_{\theta B}^I|_{\theta = 150^\circ} = K_{I,\lambda_1} f_{\theta}^I(\theta)|_{\theta = 150^\circ} = ISSF$$

$$F_{\theta B}^{II}|_{\theta = 150^\circ} = K_{II,\lambda_2} f_{\theta}^{II}(\theta)|_{\theta = 150^\circ} = ISSF$$

$$\tau_{r\theta B}|_{\theta = 150^\circ} = \frac{F_{r\theta B}^I|_{\theta = 150^\circ}}{r^{1-\lambda_1}} + \frac{F_{r\theta B}^{II}|_{\theta = 150^\circ}}{r^{1-\lambda_2}} \quad (31)$$

$$F_{r\theta B}^I|_{\theta = 150^\circ} = K_{I,\lambda_1} f_{r\theta}^I(\theta)|_{\theta = 150^\circ} = ISSF$$

$$F_{r\theta B}^{II}|_{\theta = 150^\circ} = K_{II,\lambda_2} f_{r\theta}^{II}(\theta)|_{\theta = 150^\circ} = ISSF$$

$$\sigma_{\theta B}|_{\theta = -150^\circ} = \frac{F_{\theta B}^I|_{\theta = 150^\circ}}{r^{1-\lambda_1}} - \frac{F_{\theta B}^{II}|_{\theta = 150^\circ}}{r^{1-\lambda_2}} \quad (32)$$

$$\tau_{r\theta B}|_{\theta = -150^\circ} = -\frac{F_{r\theta B}^I|_{\theta = 150^\circ}}{r^{1-\lambda_1}} + \frac{F_{r\theta B}^{II}|_{\theta = 150^\circ}}{r^{1-\lambda_2}}$$